Materials Advances

ROYAL SOCIETY OF CHEMISTRY

PAPER

View Article Online
View Journal | View Issue

Cite this: *Mater. Adv.*, 2024, 5, 6925

Design, synthesis and characterization of indolo[3,2-*a*]carbazole-based low molecular mass organogelators as hole transport materials in perovskite solar cells†

Haritha Jalaja Raghavan,[a] Nideesh Perumbalathodi,[b] Lincy Tom,[c] Kala Kannankutty,[b] Madambi Kunjukuttan Ezhuthachan Jayaraj,[de] Narayanapillai Manoj *[ae] and Tzu-Chien Wei *[bf]

Received 20th April 2024,
Accepted 17th July 2024

DOI: 10.1039/d4ma00412d

rsc.li/materials-advances

Hole transport materials (HTMs) used in third-generation perovskite solar cells (PSCs) have a significant role in enhancing power conversion efficiency (PCE). In this work, low-molecular-mass indolocarbazole-based HTMs (C_RICs) are developed as alternatives to the expensive benchmark HTM spiro-OMeTAD. These indolocarbazole-based HTMs (C_RICs) are prepared by a two-step synthesis strategy and have structural elements to control hydrophobicity, solubility, and thermal stability. The ground-state oxidation of C_RICs (−5.40 eV) matches well with the highest occupied molecular orbital (HOMO) of the perovskite (PVSK) material for efficient hole extraction similar to spiro-OMeTAD. Interestingly, the developed C_RICs exhibit excellent gelation properties in the presence of traces of water at room temperature. The gelation properties of C_RICs are expected to protect the perovskite material from deterioration by trapping the moisture when used as the HTMs in PSC devices.

1. Introduction

Perovskite solar cells (PSCs) are promising alternatives to silicon-based technology due to their strong light absorption, high ambipolar charge transport ability, long carrier diffusion length, long charge carrier lifetime, and low exciton binding energy.[1] The general PSC design consists of the perovskite (PVSK) sandwiched between hole transporting (HTM) and electron transporting (ETM) materials for efficient charge transport. A HTM facilitates efficient extraction and transport of photo-generated holes and avoids unwanted charge recombination processes, thereby enhancing the device's performance.[2,3] An ideal HTM should have improved hole mobility, high conductivity, and good solubility in a perovskite-friendly solvent and should act as a protective barrier against moisture and atmospheric oxygen.[4,5] In addition to these features, high thermal and photochemical stability, hydrophobicity, and inexpensive synthesis are desirable features of an HTM material for PSCs.[6,7] For efficient charge extraction of photo-generated holes, the highest occupied molecular orbital (HOMO) energy of a HTM must be slightly higher than the valence band edge of a light-absorbing perovskite material.[8–10] Besides the ease of synthesis, organic HTMs offer tunability of energy levels by easy incorporation of electron-donating and withdrawing substituents.[11] The commonly employed organic HTMs are 2,2′,7,7′-tetrakis[*N*,*N*-di-(*p*-methoxyphenyl)amino]-9,9′-spirobifluorene (spiro OMeTAD), poly[bis(*p*-phenyl)(2,4,6-trimethylphenyl)amine] (PTTA), poly(3,4-ethylenedioxythiophene)polystyrene sulfonate (PEDOT:PSS) *etc.*[12–14] All these materials are realized through multi-step synthesis and purification processes, thereby limiting their affordability.[15]

Low molecular mass organic materials are of great interest nowadays because of their facile route of synthesis. Hybrid heterocycles, such as indolocarbazole (IC)-based molecules, are widely used in organic electronics.[16] The desired frontier molecular orbital (FMO) levels can be achieved by structural tuning of the IC core for various applications in OLEDs and photovoltaics.[17–19] IC molecules have different structural variants based on the mode of fusion of heterocycle rings and

[a] *Department of Applied Chemistry, Cochin University of Science and Technology, Kochi-22, India. E-mail: manoj.n@cusat.ac.in*
[b] *Department of Chemical Engineering, National Tsing Hua University, 101, Section 2, Kuang Fu Road, Hsinchu, Taiwan 30013, Republic of China*
[c] *Department of Chemistry, Nirmala College, Muvattupuzha, 686661, Ernakulam, Kerala, India*
[d] *University of Calicut, Thenhipalam, Malappuram, Kerala, 673635, India*
[e] *Centre of Excellence in Advanced Materials, Cochin University of Science and Technology, Kochi-22, India*
[f] *Center for Emergent Functional Matter Science, National Yang-Ming Chiao Tung University, Hsinchu 300093, Taiwan, Republic of China. E-mail: tcwei@mx.nthu.edu.tw*

† Electronic supplementary information (ESI) available. See DOI: https://doi.org/10.1039/d4ma00412d

different structural isomers are possible for these hybrid heterocycles depending on the type of ring fusion, such as IC[2,3-*a*], IC[3,2-*a*], IC[2,3-*b*], IC[3,2-*b*], IC[2,3-*c*], IC[2,3-*h*] *etc.* Lim *et al.* developed a low-cost, environmentally stable, and highly efficient IC[2,3-*h*] hybrid-based HTM having comparable performance to spiro-OMeTAD, obtaining an efficiency of 11.6%.[20] Nazeeruddin and co-workers developed two novel HTMs, the indolo[3,2-*b*] carbazole HTM (HTM-1) and the indolo-[3,2-*a*:3′,2′-*c*]carbazole HTM (HTM-2), with a varying number of different phenylethenyl side arms, resulting in efficiencies of 13.9% and 15.2%, respectively, in PSCs.[21] Mai *et al.* used a molecule where two IC[3,2-*b*] molecules were bridged through a π-bond as a HTM and achieved an efficiency of up to 19.02%.[19]

Herein, we have designed, synthesised and characterised long alkyl chain-appended IC[3,2-*a*] based small molecules (C_RICs) as potent HTMs for PSCs. These cost-effective HTMs were synthesized using a single-step acid-catalysed condensation method. The lengthy alkyl chains were expected to control the film morphology and charge delocalization and show enhanced transport properties. Compared to a simple linear alkyl chain, the introduction of bulkier and branched alkyl chains on heterocyclic N-atoms is expected to improve optoelectronic properties.

2. Results and discussion

2.1. Synthesis and structural properties of C_RIC HTMs

The structures and schematic illustration of the synthesis of the designed C_RIC variants 1–6 are shown in Fig. 1a. C_RIC derivatives are realized by the acid-catalysed condensation reaction between the respective alkyl indoles (**7**) (2 eq.) and benzil (**8**) (1 eq.) in dry toluene under reflux conditions in the presence of *p*-toluenesulfonic acid (PTSA, 20 mol%) for 10 h.[22] The length of the alkyl group at the heterocyclic N-atom of the IC core is varied to study its effect on the film morphology and cell performance when coated on the active layers of a PSC device. The structures of these molecules were confirmed through ^{1}H NMR, ^{13}C NMR, and MALDI-TOF mass spectrometry analyses (ESI†). The single crystal X-ray diffraction data obtained for compounds 1 and 2 (Fig. 1b and c) provided unambiguous evidence for the C_RIC structures.

2.2. Single crystal analysis of C_RIC HTMs

The crystal structure determination of the compounds (C_4IC, C_8IC and C_{12}IC) was carried out to compare the conformation, packing interaction, and stability to obtain more detailed information on the structure–activity relationship. For C_{12}IC, we could not solve the structure completely due to the poor quality of the crystal despite multiple trials. The asymmetric units of compounds C_4IC, C_8IC, C_{12}IC are shown in Fig. 1b and c and Fig. S1 (ESI†), respectively. All the crystallographic data for the compounds are provided in Tables S1–S3 (ESI†). The skeleton of the molecules (except for the indolocarbazole moiety) deviates significantly from planarity. The superimposition of the geometries extracted from the crystal structures of C_4IC and C_8IC is depicted in Fig. 1d and e. The *n*-butyl groups of C_4IC (Fig. 1d) crystallize in a twisted conformation. On the other hand, *n*-octyl groups of C_8IC adopt a linear arrangement (Fig. 1e). The unit cell molecular packing structures of C_4IC and C_8IC are presented in Fig. 1f and g. The variation in the single-crystal packing should be related to the difference in alkyl chains. C_4IC exhibits a sandwich herringbone packing (Fig. 1f), whereas in C_8IC it was modified to beta packing due to the effect of alkyl chains (Fig. 1g).[23] These structural variations lead to a large decrease in the volume of beta packing of C_8IC. This means that the C_8IC molecules are packed more tightly within the layers because of the long alkyl chain substitutions. The introduction of octyl chains in C_8IC also boosted the molecular fastener (or zipper) effect and tightened the molecular packing *via* alkyl–alkyl van der Waals interaction.[24,25] However, the molecular fastener effect does not operate for C_4IC due to its twisted conformation and short alkyl chain length (Fig. 1h–j).

The interlayer spacings are calculated to be 5.2 Å and 5.1 Å, respectively, for C_4IC and C_8IC, which are too large to induce co-facial π···π interactions. The aromatic cores in both compounds are aligned with a very strong slipped π-stacking configuration. Therefore, the molecules interact mainly *via* C–H···π and van der Waals interaction. C–H···π contacts were increased as the alkyl chain length was increased. C_4IC shows favourable edge-to-face intermolecular C–H···π interactions between adjacent molecules at T-shaped contacts. The C–H···πs interactions formed between the aromatic centroid and the alkyl chain/Ph-H in C_4IC bring three neighbouring C_4IC molecules together (the shortest distance found 2.69 Å) (Fig. S2 and Table S2, ESI†). However, C–H···π interactions of C28-H28A of the butyl chain form three strong interactions with indole moieties of neighbouring C_8IC molecules (Fig. S3 and Table S3, ESI†) due to the close molecular packing (the shortest distance found 2.59 Å). These results reveal that C_8IC with long alkyl chains exhibited a more dense and stable molecular packing with a shorter distance for the neighbouring molecules. Different from the discrete dimeric sandwich packing in C_4IC, the beta packing in C_8IC molecules generates better planarity and tighter intermolecular packing, which is expected to promote the formation of uniform thin films and migration of charge carriers (Fig. 1k and l).

2.3. Theoretical studies of C_RIC HTMs

The IC-based hybrid heterocycles for HTM applications were designed based on the quantum mechanical calculations and computational simulations on a model structure C_RIC (C_1IC, R = CH_3) and other alkyl derivatives. The structure was optimized using density functional theory (DFT) at the Becke, 3-parameter, Lee–Yang–Parr (B3LYP) functional level with the 6-311G(d,p) basis set supplemented with polarization functions using Gaussian 09.[26] In the optimized geometry (Fig. 2a) of C_1IC, the dihedral angle ($G\Phi_1$) between the plane of the indolo[3,2-*a*] framework (from left) and the phenyl ring is 71° and that of the second phenyl ring ($G\Phi_2$) is 81° (Table S4, ESI†). As the length of the alkyl chains increased from C_1 to C_4, a

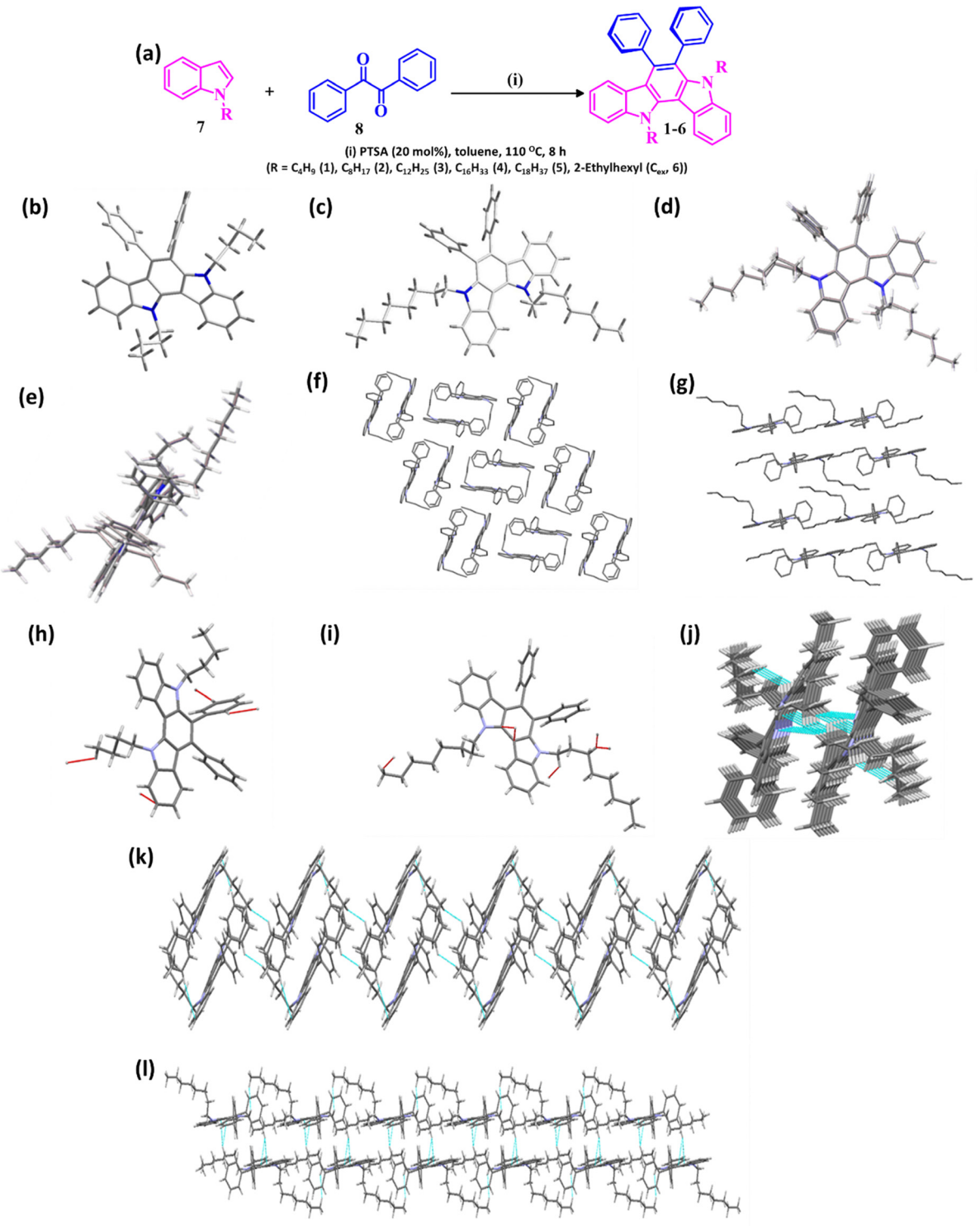

Fig. 1 (a) Scheme showing the synthesis of C_RICs, (b) and (c) the asymmetric units of C_4IC and C_8IC, (d) and (e) overlay structures of compounds C_4IC and C_8IC, (f) C_4IC with sandwich herringbone packing, (g) C_8IC with beta arrangement (H atoms are omitted for clarity), (h) and (i) short contacts arising from C_4IC and C_8IC, (j) van der Waals interaction between alkyl chains in C_8IC, (k) a supramolecular 1D chain formed by C–H···π contacts in C_4IC and (l) van der Waals interactions in C_8IC.

slight decrease in the dihedral angle was observed (Fig. 2a and b). In other words, a lengthy alkyl chain leads to more twisted phenyl rings than the model compound. A further increase in the length of the alkyl chain does not lead to more twist but a reduced twist angle for both phenyl rings, as observed in the IC derivative C_{12}IC (Fig. 2c).

The molecular electrostatic potential (ESP) refers to the overall electrostatic impact of the charge density distribution

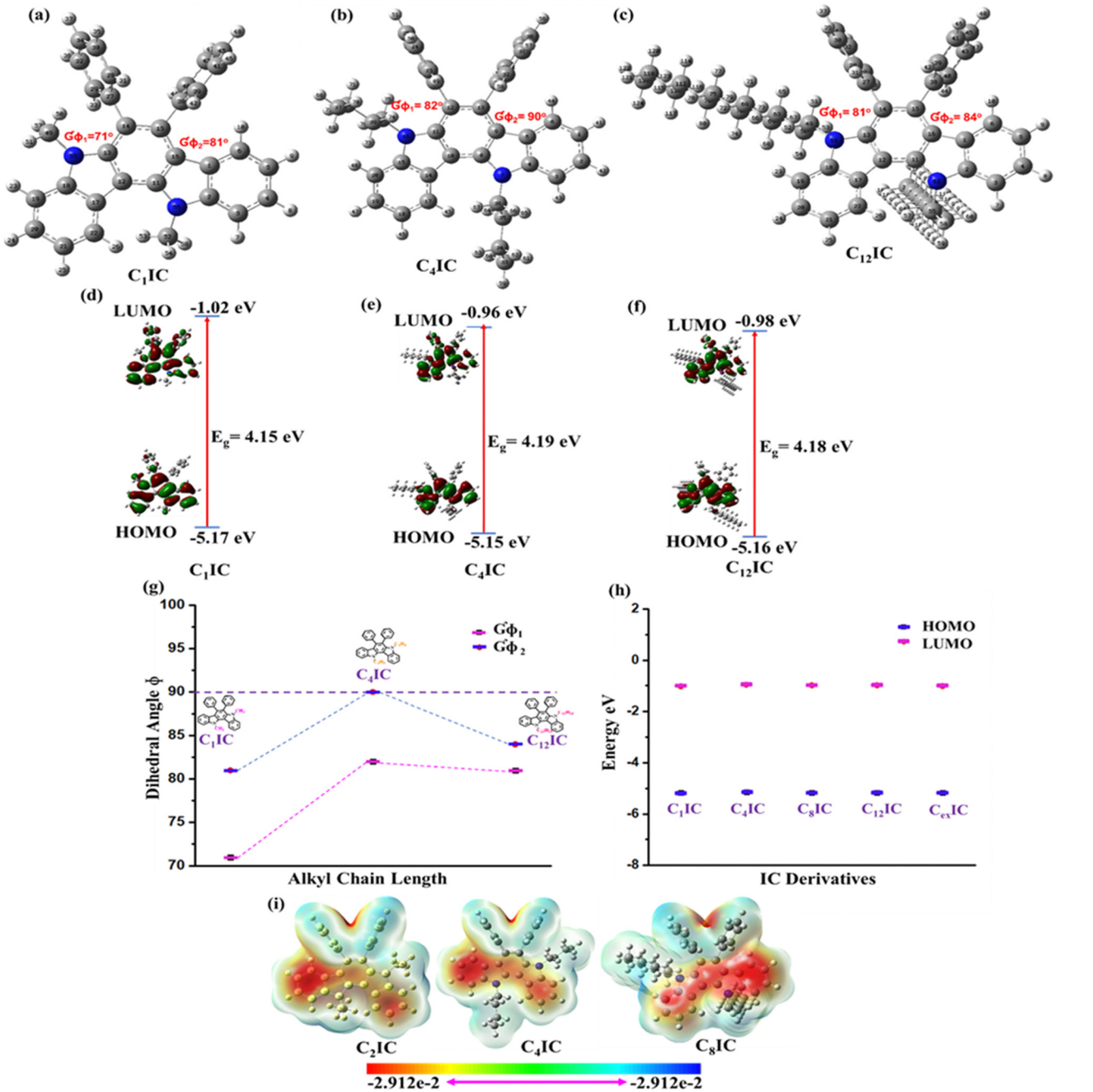

Fig. 2 Molecular model of IC derivatives: (a) C_1IC, (b) C_4IC, and (c) C_{12}IC. HOMO–LUMO plots of (d) C_1IC, (e) C_4IC, and (f) C_{12}IC. (g) Variation of dihedral angles of C_RICs with different alkyl chain lengths. (h) HOMO–LUMO energy levels of IC derivatives. (i) Total electrostatic potential (ESP) surface images of the C_RICs.

within the molecule. The computational ESP simulations were employed to examine the charge populations within the molecules.[27–29] Fig. 2i plots the ESP maps, which show the charge populations of C_RICs. The diagram portrays red regions that are electron-rich and electron-deficient regions in blue shade. The positive and negative charges on the surface can generate localized electric fields within the molecules. Therefore, it is clear from Fig. 2i that the C_RIC surfaces are completely covered by the negative charges. Thus, the ESP plots reveal the electron-rich behaviour of C_RICs, which can be considered as frugal HTMs in photovoltaic devices.

2.4. Optical and electrochemical properties

The normalized UV-vis absorption and fluorescence spectra of C_RIC HTMs together with the benchmark spiro-OMeTAD were recorded in THF solution (Fig. 3a and b), and their photophysical data are listed in Table S6 (ESI†). All C_RIC molecules exhibited blue shifted absorption bands compared with spiro-

OMeTAD and are expected to minimize parasitic absorption loss. In addition to this, the HTMs also show a blue shifted emission in the range of 386–395 nm compared with spiro-OMeTAD (416 nm). The bulkiness around the excited state destabilizes the molecules and shows a blue shift in emission in the case of C_{16}IC, C_{18}IC and C_{ex}IC. The band gaps of C_RICs are comparable with that of spiro-OMeTAD (3.26–3.29) and are calculated from the intersection between absorption and emission maxima (Fig. S4, ESI†).

A PSC with the configuration FTO/TiO_2/$FAMAPbI_3$/HTM/Au is constructed, where the active material is the mixed PVSK $FAMAPbI_3$ and the HTM is spiro-OMeTAD. For an efficient hole transport in the device following light absorption, the HOMO of the HTM should have a good band alignment with the valence band of the PVSK. As spiro-OMeTAD is the known benchmark HTM, for any HTM material to replace spiro-OMeTAD should have comparable HOMO and LUMO energy levels. DFT calculations at the ground state level in the gas phase are used to compute the HOMO and LUMO energy levels in the series of molecules that are used in the present study. The results show that the computed energy levels (Table S5, ESI†) are ideally placed to ensure an exergonic hole transport from the HOMO of the C_RICs to the HOMO of the PVSK. In the case of C_RICs, it is observed that the HOMO surface (Fig. 2d–f) indicates a distribution of total electron density largely located along the heterocyclic skeleton without significant overlap with the orthogonal phenyl rings, whereas the LUMO surface is found to be overlap with orthogonal phenyl rings. This extended LUMO surface, which is orthogonal to the plane of the heterocyclic framework, may lead to intramolecular charge transfer type absorption. However, the orthogonality of the phenyl ring makes this transition a forbidden electronic transition. Consequently, all the molecules show no absorption in the visible region of the spectrum (Table S6, ESI†), thus avoiding any inner filter effects, which is advantageous for HTM applications.

The ground state oxidation, which corresponds to the HOMO level of the HTMs, should be suitably situated to maintain the optimized balance between the hole-transfer yield and open-circuit voltage (V_{oc}) of the device.[21] Herein, the cyclic voltammogram of C_RICs in acetonitrile containing 0.1 M tetrabutylammonium hexafluorophosphate as the supporting electrolyte was recorded (Fig. 3c). From the onset potential of the anodic branch of the voltammogram, the ground state oxidation of C_RICs is estimated, which reveals the HOMO energy levels in the range of ~ -5.4 eV below the vacuum level (Table S7, ESI†). Although the HOMO levels of C_RICs are a little lower than that of the HOMO energy level of spiro-OMeTAD (-5.3 eV), these HOMO levels offer well-matched energy levels against the valence band edge of the $FAMAPbI_3$ PVSK sensitizer (-5.8 eV) and thus can facilitate efficient hole injection from the PVSK to HTM as illustrated in the energy level diagram in Fig. 3e.[30] The CV results for all C_RICs are summarized in Table S7 (ESI†). HOMO and LUMO energy levels are obtained from DFT calculations and compared with the experimental values. The corresponding LUMO energy level was estimated from the band gap and HOMO level of the C_RICs. Table S5 (ESI†) shows a

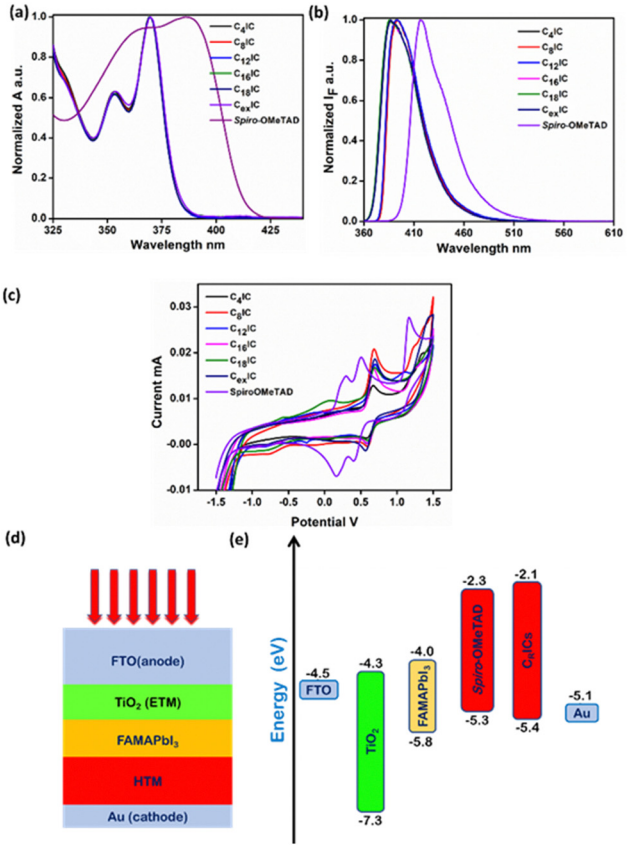

Fig. 3 (a) The absorption spectra of CRICs and spiro-OMeTAD are recorded in 10^{-5} M THF solution. (b) The photoluminescence spectra of CRICs and spiro-OMeTAD are recorded in 10^{-5} M THF solution under an ambient atmosphere. (c) Cyclic voltammogram (CV) traces of CRICs and spiro-OMeTAD. (d) Block diagram of the PSC. (e) Energy band structure of the device.

comparison of the theoretical and experimental values of HOMO and LUMO energy levels. Accurate FMO energies are challenging to obtain through DFT studies, but consistent correlations between theoretical and experimental energy values are observed. We have compared the energy levels for the C_RICs with that of the electron transport layer (ETL) in the cell design FTO/TiO_2/$FAMAPbI_3$/HTM/Au proposed for the current study. HOMO and LUMO energy levels indicate suitable band alignment with that of the band edges of the ETM and the HTM. Also, from the HOMO energy level obtained for C_RICs, we anticipated a high V_{oc} when used as the HTM in PSC devices. On the other hand, it may be noted that the higher LUMO energy levels observed can prevent electron back-transfer from the cathode to the perovskite light absorber layer through the LUMO of the HTM molecule.[2]

2.5. Thermal properties

Thermal stability of the HTMs is an important requirement for the extended life of solar cell devices fabricated using organic materials, as they are prone to changes due to high thermal stress when under solar irradiation. The thermal properties of C_RICs were examined using thermogravimetric analysis (TGA)

and differential scanning calorimetry (DSC) as shown in Fig. 4a–c and Fig. S5 (ESI†) and the data are summarized in Table S8 (ESI†). The C_RIC HTMs exhibit the degradation temperatures in the range of 356 °C to 443 °C, which are close to the degradation temperature of spiro-OMeTAD (449 °C), implying the thermal stability of the synthesized HTMs (Fig. 4a).[31] In Fig. 4b and c, we present the DSC thermograms of C_8IC and C_{12}IC, showcasing the peaks corresponding to melting for both and the glass transition process at 19 °C, while the crystallization peak is not detected for both molecules. The absence of a crystallization peak for C_RICs suggests that the presence of long alkyl chains reduces the crystallization tendency, resulting in an amorphous behavior (Fig. S5, ESI†). As we extended the alkyl chain length, we noted a decrease in the melting point of the C_RICs. This is supported by both TGA and DSC analyses, with melting peaks at T_m = 91 °C for C_8IC and T_m = 82 °C for C_{12}IC. The absence of crystallization tendency is indeed beneficial for forming better films during device fabrication and thermal annealing.[32]

2.6. Hydrophobic characteristics

High hydrophobicity is another requirement for the HTM layer as it is often the top layer below the cathode. This is essential to ward off intruding water molecules resulting from the high humidity conditions of PSCs under real deployment conditions. Penetration of water and the subsequent damage to the perovskite structure is identified as a major issue that limits the operational lifespan of PSC devices. The hydrophobic properties of thin films of C_RICs were studied by measuring their water contact angle (WCA) (Fig. 4d). The film surface displays hydrophilic properties when the contact angle is below 90° and hydrophobic properties when the contact angle exceeds 90°. Our observations indicate that C_RICs exhibit WCA values above 125°, demonstrating a high degree of hydrophobicity. In contrast, the benchmark HTM spiro-OMeTAD, with a contact angle of 80°, can be termed hydrophilic. Consequently, the superior hydrophobicity of C_RICs is likely to enhance the device's resistance to moisture penetration.

2.7. Gelation properties of C_RICs

Supramolecular assembly is an important criterion for thin-film-based electronic device production. High crystallization of HTMs in devices can limit their practical applications. Low molecular mass organic π-gelators can be used to create functional soft materials, improving carrier mobility and electron transfer efficiency.[33–35] Interestingly, gelation properties were observed for C_RICs (Table S9, ESI†) in many solvents (toluene, THF, *etc.*) and mixtures of solvents (THF–water, hexane–water,

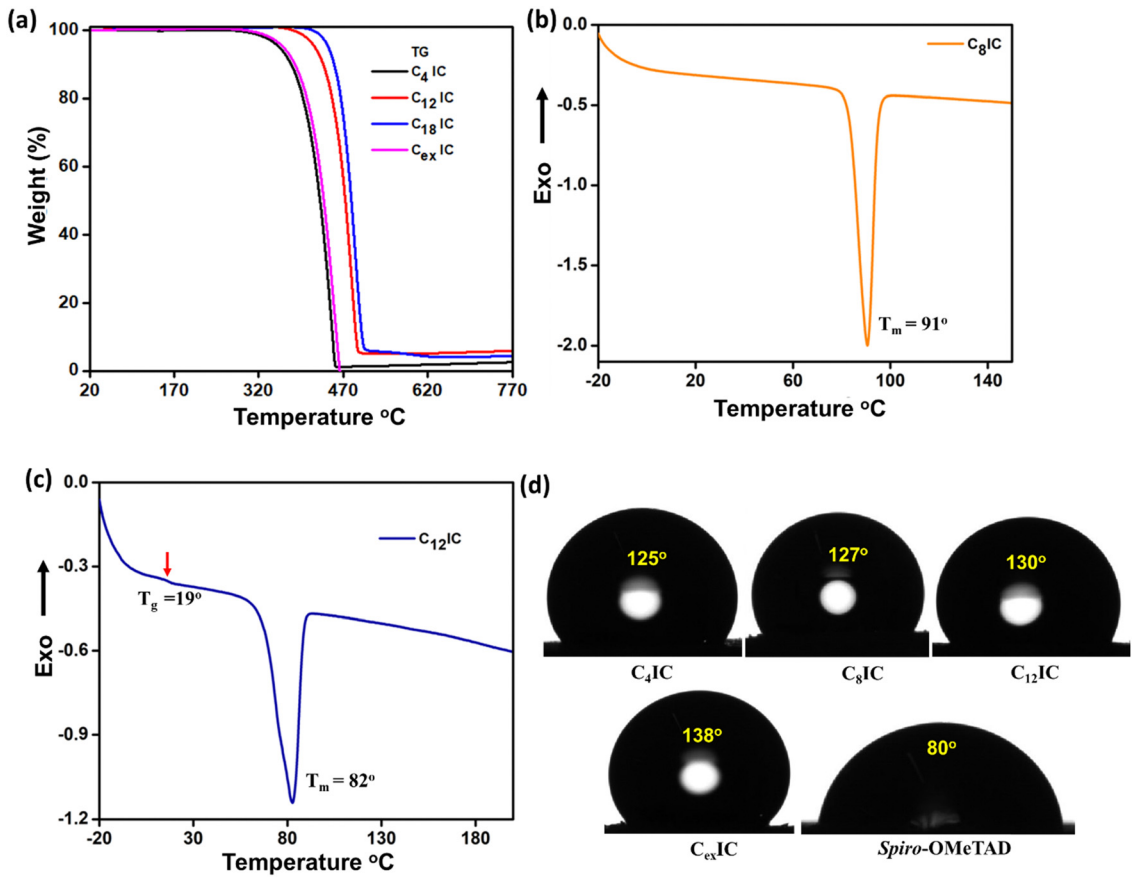

Fig. 4 (a) Thermogravimetric analysis of C_RIC HTMs under a nitrogen (N_2) atmosphere with a heating rate of 10 °C min^{-1}. (b) DSC curves of C_8IC and (c) C_{12}IC, heating rate 10 °C min^{-1}. (d) Images of contact angles showing water drop on the thin films of C_RICs.

toluene–water, *etc.*). Lengthy alkyl groups introduced at the N-positions have a crucial role in the gelation of C_RICs. Alkylation modification served two purposes initially: to weaken the strength of π–π interactions between indolocarbazole frameworks to prevent crystallisation and then to find a suitable equilibrium between solubility and precipitation in organic solvents (Fig. 5a).

These gels were transformed into transparent solutions upon heating and were reformed upon cooling along with ultrasonication.

2.8. Thin film-forming properties

The crystalline nature of C_RIC thin films is an important parameter that modulates the charge transport behaviour.[36] Thin films on an FTO substrate are prepared by spin-coating the C_RICs in chlorobenzene. The XRD patterns of the films were compared with the p-XRD patterns obtained for the powdered samples. A strong sharp signal is observed in the p-XRD patterns of both C_8IC (Fig. S6a, ESI†) and C_{12}IC (Fig. 5d), which indicates the crystalline nature of the powdered sample. However, in thin films both the samples ensured amorphous behaviour (Fig. 5e and Fig. S6b, ESI†). Furthermore, HTM materials in PSCs should be amorphous to ensure a compatible interface with the perovskite structure, facilitating more efficient charge transfer.[37]

An essential requirement for using a molecule as an HTM in PSCs is its ability to form a thin, uniform film. To achieve complete coverage over the PVSK layer, the HTM must exhibit solubility in a solvent compatible with PVSK deposition and shall possess structural components that encourage long-range order in the films. This necessity is satisfied by the presence of long *n*-alkyl chains (C_4IC, C_8IC, C_{12}IC, C_{16}IC, and C_{18}IC) and a branched chain (C_{ex}) in the heterocyclic N positions of C_RICs. The film-forming properties of C_RICs on fluorine-doped tin oxide (FTO) and PVSK films were studied by spin-coating the corresponding HTM solutions in chlorobenzene. The morphology of the resulting films was preliminarily evaluated using optical microscopy (Fig. S7a–n, ESI†). C_8IC and C_{12}IC yielded uniform films compared to spiro-OMeTAD, while the remaining HTMs resulted in non-uniform film deposition on both FTO and PVSK substrates due to their rapid crystallization. Following this preliminary analysis using optical microscopy, the nanostructures of C_4IC, C_8IC, and C_{12}IC films over PVSK and glass films were further characterized using atomic force microscopy (AFM). The film morphologies were compared based on AFM images (Fig. 6a–j). The different heights observed in AFM images can be correlated to the varying surface roughness (S_a) of films on different substrates. These AFM images validated the film-forming nature of different HTMs on PVSK and FTO surfaces. They indicated that the PVSK surface appeared smoother (S_a = 15.97 nm) than the FTO surface (S_a = 20.99 nm) due to the relatively larger grain size of FTO on glass. It is also evident from the AFM images that the film-forming nature of the C_RIC HTMs is independent of the substrate's roughness; whether on a smoother PVSK or on a relatively rougher FTO substrate, each C_RIC derivative tends to show its characteristic film formation ability.

The AFM images (Fig. 6d and e) revealed that C_8IC and C_{12}IC displayed smooth films over the PVSK, with surface roughness (S_a) values of 0.66 nm and 0.53 nm, respectively, which are smoother than that of spiro-OMeTAD (S_a = 4.07 nm). In contrast, C_4IC (Fig. 6c) resulted in a non-uniform and relatively rough film (S_a = 33.15 nm) due to its short *n*-alkyl chain leading to rapid crystallization. These findings indicate that

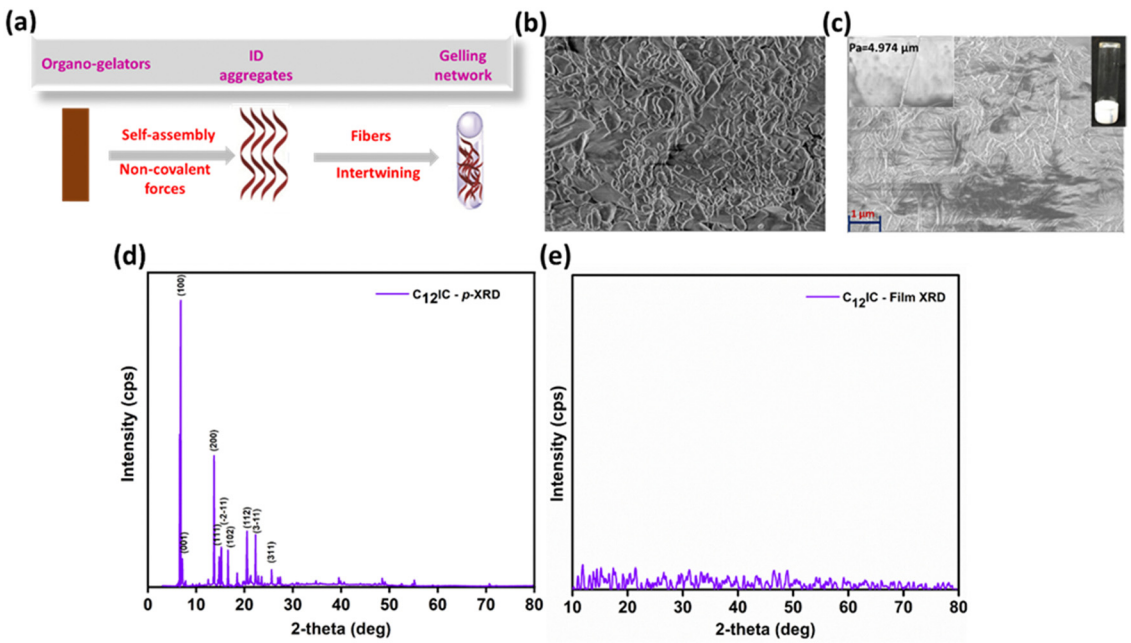

Fig. 5 (a) Graphical representation of gelation processes, (b) FESEM lengthy alkyl groups introduced image of a powdered C_{12}IC organo-gelator, (c) FESEM image of a C_{12}IC xerogel, (d) X-ray diffraction patterns of powder samples of C_{12}IC, and (e) thin film samples of C_{12}IC on an FTO substrate.

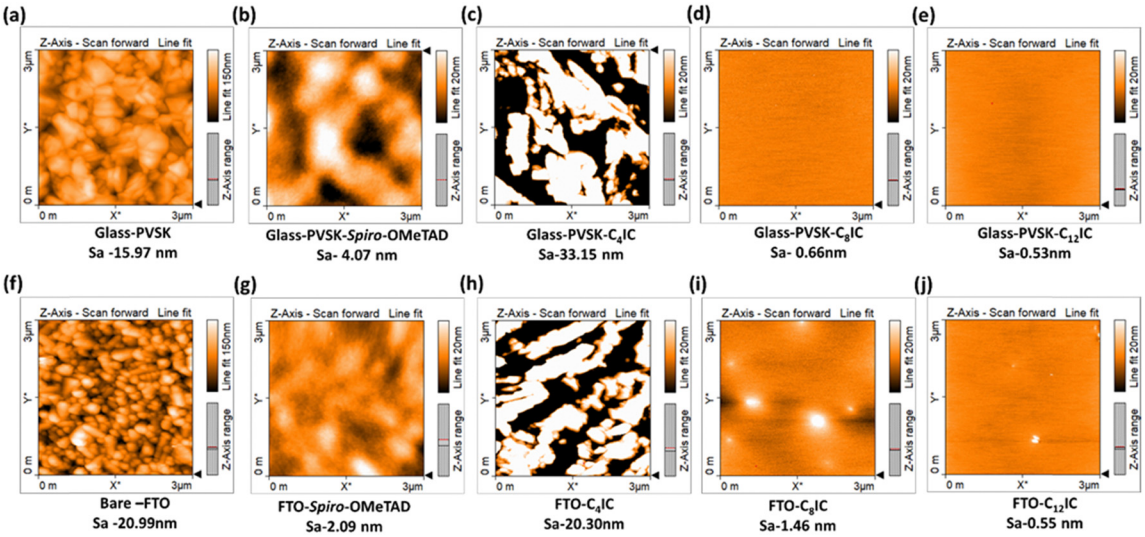

Fig. 6 AFM images of C_RICs and spiro-OMeTAD films on FTO and PVSK films: (a) glass/PVSK, (b) glass/PVSK/spiro-OMeTAD, (c) glass/PVSK/C_4IC, (d) glass/PVSK/C_8IC, (e) glass/PVSK/C_{12}IC, (f) bare FTO, (g) FTO/spiro-OMeTAD, (h) FTO/C_4IC, (i) FTO/C_8IC, and (j) FTO/C_{12}IC.

the film-forming nature of HTMs is highly dependent on their molecular structure. For example, the C_4IC HTM, with shorter alkyl chains, tends to crystallize quickly, resulting in a rough film, whereas increasing the alkyl chain length transforms the crystalline nature to an amorphous one, thereby enhancing the film-forming ability of the HTM. Furthermore, the visible light transmission characteristics of these HTM thin films on the FTO substrate are studied using UV-visible absorption spectroscopy. The transmittance spectra of the C_RIC thin films are comparable or better than those of spiro-OMeTAD thin films (Fig. S8, ESI†). A worthy observation is that thin films of C_RIC derivatives do not absorb visible light as spiro-OMeTAD does. This property can be beneficial for reducing the visible light filtering effect when compared to spiro-OMeTAD based PSCs. The spin coated films of C_RICs were subjected to annealing at 110 °C, and the resultant films were again analysed by optical and AFM microscopies as well as by UV-vis spectroscopy to confirm structural integrity. These studies showed no changes in the film morphology or electronic properties, suggesting that these films possess thermally stable behaviour.

2.9. Opto-electronic properties of C_RIC HTMs

After optimizing the film-forming properties, we obtained a smooth film for C_8IC and C_{12}IC, so we further proceeded with the investigation of the optical properties of C_8IC and C_{12}IC. The hole extraction efficiency of C_RIC HTMs was evaluated by using steady-state photoluminescence (SSPL) spectra of PVSK/C_RIC HTMs. The observed decrease in photoluminescence (PL) intensity upon the introduction of the C_RIC HTMs on the PVSK indicates effective hole extraction from the oxidized PVSK to C_RIC HTMs (Fig. 7a), which is attributed to favourable valence band (VB) alignment (Fig. 3d). Among the studied HTMs, C_{12}IC exhibited a slightly higher PL quenching, suggesting a better hole extraction compared to C_8IC. This could be due to the better film-forming ability of C_{12}IC, facilitating improved charge transport within the device architecture.

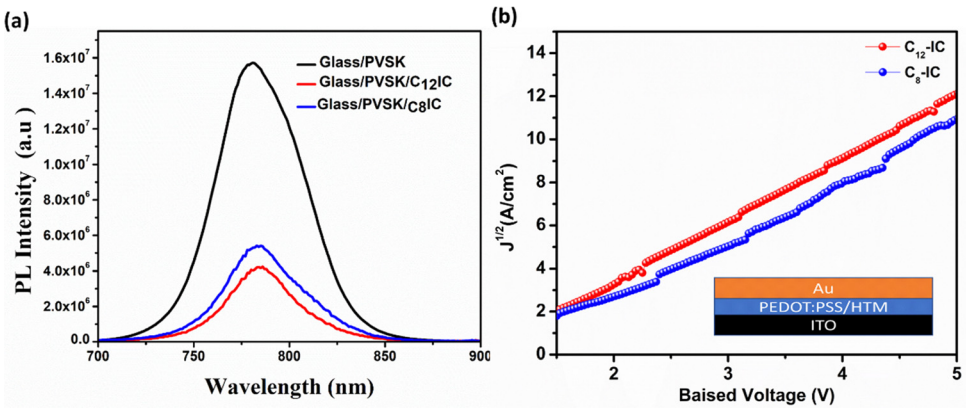

Fig. 7 (a) SSPL of glass/PVSK, glass/PVSK/C_{12}-IC, and glass/PVSK/C_8-IC films respectively. (b) SCLC curves of C_RIC HTMs.

Hole mobilities of the C_RIC HTMs are estimated using the space-charge limited current (SCLC) method by fabricating the hole-only devices (FTO/PEDOT/HTM/Au) following the Mott–Gurney law. The dark *J–V* characteristics of hole-only devices were analysed, with the SCLC curve fitted according to the Mott–Gurney law:[38]

$$(J) = \frac{9}{8}\mu\varepsilon\varepsilon_0\frac{v^2}{d^3}$$

where J is the current density, ε is the permittivity of the organic material (3), ε_0 is the vacuum permittivity (8.85×10^{-12} F m^{-1}), μ is the hole mobility, V is the applied voltage, and d is the thickness of the film. The obtained hole mobility values of the C_RICs were 1.30×10^{-4} cm^2 V^{-1} s^{-1} for C_{12}IC and 1.15×10^{-4} cm^2 V^{-1} s^{-1} for C_8IC respectively. These values are consistent with the literature values reported for HTMs used in PSCs (1.47×10^{-4} cm^2 V^{-1} s^{-1} for spiro-OMETAD).[39–42]

A device (FTO/TiO_2/$FAMAPbI_3$/HTM/Au) was fabricated using un-doped C_RICs (C_8IC and C_{12}IC) as HTMs. The current density–voltage (*J–V*) characteristics and the efficiency of the fabricated device were evaluated. The *J–V* characteristics of undoped C_8IC and C_{12}IC were measured and compared to those of doped spiro-OMeTAD (doped with lithium bis(trifluoromethanesulfonyl)imide (LiTFSI) and 4-*tert*-butylpyridine (tBP)). The *J–V* curve obtained is shown in Fig. S9 (ESI†). The efficiency of the fabricated device was calculated, and the results are summarized in Table S10 (ESI†). Analysis of the device parameters indicates that performance improvements are necessary. Further optimization of the device parameters is currently in progress.

Table S10 (ESI†) shows that C_RIC based PSCs currently exhibit inferior photovoltaic performance. However, space-charge-limited current (SCLC) hole mobility measurements and photoluminescence (PL) studies have demonstrated that C_RIC HTMs possess highly desirable optoelectronic properties, including sufficient hole mobility (1.30 to 1.15×10^{-4} cm^2 V^{-1} s^{-1}) and enhanced hole extraction from the PVSK layer. The observed inferior performance of this class of HTMs can primarily be attributed to their non-uniform film formation, resulting from limited solubility in PVSK-friendly solvents such as chlorobenzene (CB), toluene, and isopropyl alcohol (IPA).

In this study, we embarked on a comprehensive evaluation of the facile synthetic routes for different C_RIC derivatives. We thoroughly examined their physical and electronic properties, focusing on their potential as HTMs in PSCs. We are currently addressing the challenges associated with thin film formation through innovative and aggressive approaches. Additionally, we are actively developing methods to fabricate C_RIC thin film-based HTMs *via* thermal deposition techniques. Our thermal stability analysis has revealed that these materials exhibit robust stability, making them excellent candidates for thermal evaporation.

3. Conclusions

In this study, C_RICs, low molecular mass molecules, were designed, synthesized, and characterized for use as potential HTMs for PSCs. The simple and easy purification of these materials makes them cost-effective and scalable. They show absorption characteristics in the UV region of the spectrum. p-XRD data revealed the crystalline nature of the powdered sample, while in the case of films, these molecules show amorphous characteristics, which would be beneficial for better film formation during device fabrication. Quantum chemistry simulations and DFT studies support their comparable HOMO and LUMO energy levels with those of the benchmark spiro-OMeTAD. In addition to this, C_RICs possess competitive thermal, electrochemical, and optoelectronic properties along with film-forming properties in relation to spiro-OMeTAD. Furthermore, introducing long alkyl chains on the N of indolocarbazole systems can induce gelation with a small amount of water, potentially shielding the perovskite material from moisture damage while it is part of the device. Hole mobilities were studied and found to be comparable with that of spiro-OMeTAD and a PSC device having the FTO/TiO_2/$FAMAPbI_3$/HTM/Au structure was fabricated and studied, but the efficiencies obtained were low compared to the device fabricated using spiro-OMeTAD. All these studies show that the hydrophobic nature coupled with the water gelation properties and suitable electronic structures can make C_RICs important components of future PSC devices. The promising findings of our research underscore the immense potential of C_RIC based HTMs in PSC applications. We believe that with further refinement, these materials can overcome their current limitations and significantly enhance the performance of PSCs. Our ongoing efforts aim to optimize these techniques and fully harness the capabilities of C_RIC based HTMs.

Author contributions

This work is part of the PhD thesis work of HJR. LT did s-XRD analysis. NP, KK, and TCW studied thin film properties and are the international collaborators. TCW, MKJ and NM are group leaders and conceptualised the work.

Data availability

The data supporting this article have been included as part of the ESI.†

Conflicts of interest

There are no conflicts of interest to declare.

Note added after first publication

This article replaces the version published 23rd July 2024, which contained errors within an equation in section 2.9.

Acknowledgements

H. J. R. gratefully acknowledges the University Grants Commission (UGC) for the research fellowship (55/(OBC) (CSIR-UGC NET DEC.2016)). N. M., M. K. J. and T. C. W. are thankful to DST – GITA (GITA/DST/TWN/p-85/2019) for financial support. The authors are grateful to National Tsing Hua University (NTHU), Taipei, DST-SAIF Cochin, IUCND CUSAT, CAM CUSAT, Department of Polymer Science and Rubber Technology CUSAT, and Department of Physics CUSAT for facilities.

References

1 S. Kazim, M. K. Nazeeruddin, M. Grätzel and S. Ahmad, *Angew. Chem., Int. Ed.*, 2014, **53**, 2812–2824.
2 X. Liang, K. Wang, R. Zhang, K. Li, X. Lu, K. Guo, H. Wang, Y. Miao, H. Xu and Z. Wang, *Dyes Pigm.*, 2017, **139**, 764–771.
3 L. Zhu, Y. Shan, R. Wang, D. Liu, C. Zhong, Q. Song and F. Wu, *Chem. – Eur. J.*, 2017, **23**, 4373–4379.
4 W.-J. Chi, Q.-S. Li and Z.-S. Li, *Synth. Met.*, 2016, **211**, 107–114.
5 A. Michaleviciute, M. Degbia, A. Tomkeviciene, B. Schmaltz, E. Gurskyte, J. V. Grazulevicius, J. Bouclé and F. Tran-Van, *J. Power Sources*, 2014, **253**, 230–238.
6 G. Sathiyan, E. Sivakumar, R. Ganesamoorthy, R. Thangamuthu and P. Sakthivel, *Tetrahedron Lett.*, 2016, **57**, 243–252.
7 X. Yin, L. Guan, J. Yu, D. Zhao, C. Wang, N. Shrestha, Y. Han, Q. An, J. Zhou and B. Zhou, *Nano Energy*, 2017, **40**, 163–169.
8 L. G. Kudriashova, D. Kiermasch, P. Rieder, M. Campbell, K. Tvingstedt, A. Baumann, G. V. Astakhov and V. Dyakonov, *J. Phys. Chem. Lett.*, 2017, **8**, 4698–4703.
9 Y. Li, Y. Li, J. Shi, H. Li, H. Zhang, J. Wu, D. Li, Y. Luo, H. Wu and Q. Meng, *Appl. Phys. Lett.*, 2018, 112.
10 N. F. Montcada, J. M. Marín-Beloqui, W. Cambarau, J. Jimenez-Lopez, L. Cabau, K. T. Cho, M. K. Nazeeruddin and E. Palomares, *ACS Energy Lett.*, 2017, **2**, 182–187.
11 G.-W. Kim, G. Kang, J. Kim, G.-Y. Lee, H. I. Kim, L. Pyeon, J. Lee and T. Park, *Energy Environ. Sci.*, 2016, **9**, 2326–2333.
12 Z. H. Bakr, Q. Wali, A. Fakharuddin, L. Schmidt-Mende, T. M. Brown and R. Jose, *Nano Energy*, 2017, **34**, 271–305.
13 A. Kojima, K. Teshima, Y. Shirai and T. Miyasaka, *J. Am. Chem. Soc.*, 2009, **131**, 6050–6051.
14 Y.-K. Wang, Z.-Q. Jiang and L.-S. Liao, *Chin. Chem. Lett.*, 2016, **27**, 1293–1303.
15 I. M. Abdellah, T. H. Chowdhury, J.-J. Lee, A. Islam and A. El-Shafei, *Sol. Energy*, 2020, **206**, 279–286.
16 C. C. Lai, M. J. Huang, H. H. Chou, C. Y. Liao, P. Rajamalli and C. H. Cheng, *Adv. Funct. Mater.*, 2015, **25**, 5548–5556.
17 R. A. Irgashev, N. A. Kazin, G. L. Rusinov and V. N. Charushin, *ARKIVOC*, 2018, **2018**, 203–220.
18 S. Lengvinaite, J. Grazulevicius and S. Grigalevicius, *Synth. Met.*, 2009, **159**, 91–95.
19 R. Mai, X. Wu, Y. Jiang, Y. Meng, B. Liu, X. Hu, J. Roncali, G. Zhou, J.-M. Liu and K. Kempa, *J. Mater. Chem. A*, 2019, **7**, 1539–1547.
20 I. Lim, E.-K. Kim, S. A. Patil, W. Lee, N. K. Shrestha, J. K. Lee, W. K. Seok, C.-G. Cho and S.-H. Han, *RSC Adv.*, 2015, **5**, 55321–55327.
21 I. Petrikyte, I. Zimmermann, K. Rakstys, M. Daskeviciene, T. Malinauskas, V. Jankauskas, V. Getautis and M. K. Nazeeruddin, *Nanoscale*, 2016, **8**, 8530–8535.
22 V. Nair, V. Nandialath, K. G. Abhilash and E. Suresh, *Org. Biomol. Chem.*, 2008, **6**, 1738–1742.
23 D. Loveland, B. Kailkhura, P. Karande, A. M. Hiszpanski and T. Y.-J. Han, *J. Chem. Inf. Model.*, 2020, **60**, 6147–6154.
24 H. Inokuchi, G. Saito, P. Wu, K. Seki, T. B. Tang, T. Mori, K. Imaeda, T. Enoki, Y. Higuchi and K. Inaka, *Chem. Lett.*, 1986, **15**, 1263–1266.
25 M. J. Kang, I. Doi, H. Mori, E. Miyazaki, K. Takimiya, M. Ikeda and H. Kuwabara, *Adv. Mater.*, 2011, **23**, 1222–1225.
26 K. S. Keremane, I. M. Abdellah, P. Naik, A. El-Shafei and A. V. Adhikari, *Phys. Chem. Chem. Phys.*, 2020, **22**, 23169–23184.
27 A. Mahmood, J.-Y. Hu, B. Xiao, A. Tang, X. Wang and E. Zhou, *J. Mater. Chem. A*, 2018, **6**, 16769–16797.
28 J.-M. Park, D. W. Kim, H. Y. Chung, J. E. Kwon, S. H. Hong, T.-L. Choi and S. Y. Park, *J. Mater. Chem. A*, 2017, **5**, 16681–16688.
29 J. Wójcik, J. Peszke, A. Ratuszna, P. Kuś and R. Wrzalik, *Phys. Chem. Chem. Phys.*, 2013, **15**, 19651–19658.
30 N. Perumbalathodi, T. S. Su and T. C. Wei, *Adv. Mater. Interfaces*, 2022, **9**, 2201191.
31 K. S. Keremane, P. Naik and A. V. Adhikari, *J. Nano Electron. Phys.*, 2020, **12**, 02039.
32 T. Malinauskas, D. Tomkute-Luksiene, R. d Sens, M. Daskeviciene, R. Send, H. Wonneberger, V. Jankauskas, I. Bruder and V. Getautis, *ACS Appl. Mater. Interfaces*, 2015, **7**, 11107–11116.
33 H. Ebata, T. Izawa, E. Miyazaki, K. Takimiya, M. Ikeda, H. Kuwabara and T. Yui, *J. Am. Chem. Soc.*, 2007, **129**, 15732–15733.
34 S. Wakim, J. Bouchard, M. Simard, N. Drolet, Y. Tao and M. Leclerc, *Chem. Mater.*, 2004, **16**, 4386–4388.
35 J. Yu, J. Luo, Q. Chen, K. He, F. Meng, X. Deng, Y. Wang, H. Tan, H. Jiang and W. Zhu, *Tetrahedron*, 2014, **70**, 1246–1251.
36 W. Zhang, M. Saliba, D. T. Moore, S. K. Pathak, M. T. Hörantner, T. Stergiopoulos, S. D. Stranks, G. E. Eperon, J. A. Alexander-Webber and A. Abate, *Nat. Commun.*, 2015, **6**, 6142.
37 T. Yeşil, A. Mutlu, S. Siyahjani Gültekin, Z. G. l Günel and C. Zafer, *ACS Omega*, 2023, **8**, 27784–27793.
38 H. J. Snaith and M. Grätzel, *Appl. Phys. Lett.*, 2006, **89**, 262114.

39 P. Worakajit, T. Sudyoadsuk, V. Promarak, A. Saeki and P. Pattanasattayavong, *J. Mater. Chem. C*, 2021, **9**, 10435–10442.
40 J. Y. Park, S. L. Kwak, H. J. Park and D.-H. Hwang, *Nanomaterials*, 2023, **13**, 1934.
41 L. Wan, Y. Zhao, Y. Tan, L. Lou and Z.-S. Wang, *Chem. Eng. J.*, 2023, **455**, 140569.
42 T.-S. Su, H.-Y. Tsai, K. Kannankutty, C.-T. Chen, Y. Chi and T.-C. Wei, *Sol. RRL*, 2019, **3**, 1900143.